Exploring Quasar Variability in Gravitational Lensing with the Roman Telescope

Esmeralda Guliqani[1], Lindita Hamolli[2], Mimoza Hafizi[2]
[1] Department of Mathematics and Physics, Faculty of Natural and Human Sciences, "Fan S. Noli" University of Korça, 7001 Korça, Albania
[2] Department of Physics, Faculty of Natural Sciences, University of Tirana, 1001 Tirana, Albania
eguliqani@unkorce.edu.al
(Submitted on 27.05.2025; Accepted on 16.06.2025)

Abstract. Gravitational lensing of quasars is a powerful tool for probing cosmological parameters and the internal structure of quasars. In particular, time delays between multiple lensed images provide key constraints on the Hubble constant (H_0), contributing to ongoing efforts to resolve the Hubble tension. Using simulated observations from the upcoming Roman Space Telescope, we investigate the impact of flare-induced perturbations on the light curves and time delays of lensed quasar images. Through Monte Carlo simulations, we construct quasar-galaxy systems based on observed redshift distributions and galaxy mass-luminosity functions. Modeling the lensing effect with the Singular Isothermal Ellipsoid (SIE) profile, we examine double, triple, and quadruple quasar configurations. For each case, we compute angular separations, time delays, and time delay differences. Our analysis reveals that within a flare distance range of 10 to 1000 pc, intrinsic quasar variability caused by flares can disrupt correlations between lensed images. Specifically, 22.41% of double quasars and 9.52% of quadruple quasars exhibit no correlation between their light curves due to flare activity. These multiple time delays introduce uncertainties that may impact the precision of cosmological parameter measurements, particularly the determination of H_0. These findings underscore the necessity of accounting for quasar variability when applying time-delay cosmography.
Key words: quasar, elliptical galaxy, strong lensing, time delay.

Introduction

Quasar lensing is a gravitational phenomenon that occurs when a galaxy or a group of galaxies lies between the observer and a quasar, causing light to bend and form multiple distorted images. This effect, known as gravitational lensing, provides a unique opportunity to study distant quasars and their environments. One of the most significant applications of quasar lensing is the measurement of gravitational time delays (Refsdal, 1964), which refer to the differences in light travel time between multiple strongly lensed images of the same quasar. These time delays serve as powerful tools for probing cosmological parameters, particularly in constraining the Hubble constant, H_0 (Schechter, 2004).

Today, different measurement techniques have led to discrepancies in the estimated values of H_0, a conflict known as Hubble's tension. The SHOES collaboration, which combines Cepheid variables, Type Ia supernovae, and parallax measurements to determine distances within the Hubble flow, has reported a value of $H_0 = 73 \pm 1 \mathrm{km\,s^{-1}Mpc^{-1}}$ (Riess et al., 2021). In contrast, measurements based on Cosmic Microwave Background (CMB) radiation have yielded a lower value of $H_0 = 67.4 \pm 0.5$ $\mathrm{km\,s^{-1}Mpc^{-1}}$ (Aghanim et al., 2020). Meanwhile, the H0LiCOW collaboration, utilizing the time delay method in gravitational lensing studies, has found $H_0 = 73.3^{+1.7}_{-1.8}$ $\mathrm{km\,s^{-1}Mpc^{-1}}$ (Wong et al., 2020). These results highlight the existing variations in Hubble constant estimates, emphasizing the need for precise time delay measurements in

gravitational lensing systems. Upcoming telescopes will play a crucial role in refining these measurements, helping to place strong constraints on cosmological parameters and improve our understanding of the Universe's expansion. Cosmological surveys such as the Vera Rubin Observatory's Legacy Survey of Space and Time (LSST) (Oguri & Marshall, 2010) and the Roman Nancy Grace Space Telescope (Spergel et al., 2015; Hamolli et al., 2023a) will significantly expand the catalog of gravitationally lensed quasars. Generally, the lensed quasars appear as double, triple, or quadruple systems, providing additional opportunities to study quasar morphology and dynamics. One of the galaxy models that enables such studies is the singular isothermal ellipsoid galaxy (SIE) (Guliqani et al., 2024).

Quasars, in addition to being affected by strong lensing from the entire lensing galaxy, also experience microlensing effects caused by compact objects within the lensing galaxy. As known from observations, quasars possess a complex internal structure, consisting of a central black hole, an accretion disk, a Broad Line Region, a surrounding dust torus, and a Narrow Line Emission Region. These inner components can be studied through microlensing-induced variations in their light curves (Vernardos et al., 2023). Both quasar lensing and microlensing provide valuable insights into the internal structure of quasars. Simulations conducted by Yonehara et al. (1998, 1999) demonstrate how multiwavelength observations can reveal intricate details of quasar accretion disks, offering a deeper understanding of their physical properties.

In general, one of the most common phenomena observed in quasars is their frequent flare activity, which introduces variability independent of gravitational lensing effects. Observations from the Hubble Space Telescope have confirmed the presence of flares in quasar regions extending over 10^2 to 10^3 parsecs, consistent with previous studies of nearby quasars (Bahcall et al., 1997).

In this paper, we follow the ideas of Yonehara (1999) and Goicoechea (2002) to investigate how outburst events affect the correlation between observed light curves of lensed quasars. This analysis is particularly relevant for future observations with the Roman Space Telescope, which will provide high-resolution data to refine our understanding of quasar variability and gravitational lensing effects. The Roman Space Telescope is a NASA infrared observatory designed to be positioned at the second Lagrangian point (L2) of the Earth-Sun system. It will facilitate a broad range of astrophysical investigations, spanning from Solar System studies to cosmology, utilizing two primary instruments: the Wide Field Instrument (WFI) and the Coronagraph Instrument. With an angular resolution of 0.1 arcseconds and an imaging cadence of 5 days (Beaton et al., 2023), it will provide high-precision observations. We utilize its capabilities to determine the detection limits for identifying correlations in the light curves of lensed quasar images, which are expected to be observed by the Roman Space Telescope.

The paper is structured as follows: Section 2 provides an overview of gravitational lensing, detailing the calculation of time delays and time delay differences between images within the Singular Isothermal Ellipsoid (SIE) lens model. Section 3 presents the simulations and results obtained for this lens model. Finally, Section 4 summarizes the key conclusions of the study.

1. A Review of the Basics of Gravitational Lensing

The gravitational field of a massive object (the lens) distorts the path of light from a distant source (quasar), forming multiple images, arcs, or rings. This phenomenon is called strong gravitational lensing. The positions of the multiple images are the solutions of the lens equation (Kormann et al., 1994; Meneghetti, 2021). Its dimensionless form is

$$\mathbf{y} = \mathbf{x}_i - \alpha(\mathbf{x}_i). \tag{1}$$

In this equation $\mathbf{y}$ represents the dimensionless position of the source, $\mathbf{x}_i$ is the dimensionless position of the i-th image and $\alpha(\mathbf{x}_i)$ is the scaled deflection angle of the i-th image. An image in the form of a ring, called an Einstein ring, is formed when the source, lens, and observer are perfectly aligned ($\mathbf{y} = 0$). The radius of this ring is given by

$$\xi_0 = \sqrt{\frac{4GMD_{LS}D_L}{c^2 D_S}}. \tag{2}$$

Here: G is the gravitational constant, c is the speed of light in vacuum, M is the mass of the lens inside Einstein radius, D_{LS} is the angular diameter distance from the lens to the source, D_L is the angular diameter distance from the lens to the observer, and D_S the angular diameter distance from the source to the observer.

To produce multiple images for certain source positions, the convergence $\kappa = \sum(\xi)/\sum_{crit}$, where $\sum(\xi)$ is surface mass density at position ξ and $\sum_{crit} = \frac{c^2}{4\pi G}\frac{D_S}{D_{LS}D_L}$ is the critical surface mass density, must satisfy $\kappa \geq 1$.

Since quasars are located very far from the observer in strong lensing events, they are considered point sources. If a quasar is gravitationally lensed into two images located at positions $\mathbf{x}_i$ and $\mathbf{x}_j$ in the lens plane, the relative time delay between them can be measured and is given by

$$\Delta t_{i-j}(\mathbf{y}) = \frac{(1+z_l)}{c}\frac{D_S\xi_0^2}{D_L D_{LS}}\left[\Phi(\mathbf{x}_i, \mathbf{y}) - \Phi(\mathbf{x}_j, \mathbf{y})\right], \tag{3}$$

where z_l is the redshift of the lens, $\Phi(\mathbf{x}_i, \mathbf{y}) = \frac{1}{2}(\mathbf{x}_i - \mathbf{y})^2 - \Psi(\mathbf{x}_i)$ is the Fermat potential (Kormann et al., 1994; Meneghetti, 2021), and $\Psi(\mathbf{x}_i)$ the scaled lensing potential of the lens. This potential is related to the scaled deflection angle by $\alpha(\mathbf{x}_i) = \nabla\Psi(\mathbf{x}_i)$.

Considering a finite-size perturbation or a flare occurring in the surrounding region of the source at $\mathbf{y} + \delta\mathbf{y}$, it results in a disturbance in the position of the lensed image at $\mathbf{x}_i + \delta\mathbf{x}_i$ in the lens plane, following the lens equation

$$\mathbf{y} + \delta\mathbf{y} = \mathbf{x}_i + \delta\mathbf{x}_i + \alpha(\mathbf{x}_i + \delta\mathbf{x}_i),\ i = 1,\ 2,\ 3,\ or\ 4. \tag{4}$$

By subtracting equation (4) from equation (1), applying a Taylor expansion to $\alpha(\mathbf{x}_i)$, and neglecting higher-order terms ($\delta\mathbf{y} \ll \mathbf{y}, \delta\mathbf{x}_i \ll \mathbf{x}_i$) (Hamolli et al., 2024), the time delay difference can be expressed as

$$\delta(\Delta t) = \Delta t(\mathbf{y} + \delta\mathbf{y}) - \Delta t(\mathbf{y}). \tag{5}$$

1.2. The Singular Isothermal Ellipsoid (SIE) Lens Model

In a previous paper (Hamolli et al., 2024), we studied the capabilities of the Roman Space Telescope to investigate the correlation between the light curves, which are induced by the finite source size of variability for two galaxy models: the Singular Isothermal Sphere (SIS) and the Non-Singular Isothermal Sphere (NIS). Similarly, in this paper, we will extend the analysis to the elliptical case, focusing on the Singular Isothermal Ellipsoid. A singular isothermal ellipsoid galaxy is a lens model with surface mass density

$$\Sigma\left(\xi\right)=\frac{\sigma^{2}}{2G}\frac{\sqrt{f}}{\sqrt{\xi_{1}^{2}+f^{2}\xi_{2}^{2}}}, \tag{6}$$

where σ is velocity dispersion, ξ_1 and ξ_2 are two axes in the plane of the lens, and f is the axis ratio of the ellipse $0<f\leq 1$. The semi-major axis of the ellipse (galaxy) is along ξ_2. For this lens model, the potential is the solution of the Poisson equation $\nabla^2\Psi=2\kappa$ (Kormann et al., 1994). The condition $\kappa\geq 1$, which allows for the formation of multiple images, is satisfied for a potential $\Psi(x_i,\varphi_i)$ described in polar coordinates (x,φ) as follows

$$\Psi\left(x_{i},\varphi_{i}\right)=x_{i}\frac{\sqrt{f}}{f^{'}}\left[\sin\varphi_{i}\arcsin\left(f^{'}\sin\varphi_{i}\right)+\cos\varphi_{i}\arcsin h\left(\frac{f^{'}}{f}\cos\varphi_{i}\right)\right] \tag{7}$$

where $f^{'}=\sqrt{1-f^{2}}$. The lens equation for SIE model of the lens can be written as (Kormann et al., 1994; Meneghetti, 2021)

$$y_{1}=x_{i}\cos\varphi_{i}-\frac{\sqrt{f}}{f^{'}}\arcsin h\left(\frac{f^{'}}{f}\cos\varphi_{i}\right) \tag{8}$$

$$y_{2}=x_{i}\sin\varphi_{i}-\frac{\sqrt{f}}{f^{'}}\arcsin\left(f^{'}\sin\varphi_{i}\right) \tag{9}$$

here, y_1 and y_2 are the coordinates of the source and the components of the deflection angle $(\alpha_{1i},\alpha_{2i})$ are found as the gradient of the potential $(\alpha(\mathbf{x})=\nabla\Psi(\mathbf{x}))$. For a specific source position (y_1,y_2), we utilize the lens equation to determine the polar coordinates of the images, expressed as (x_i,φ_i). Brent's method (Brent, 1971) is employed in Python to compute these coordinates. The lens equation can produce one, two, three, or four images depending on the source position relative to the galaxy, the axis ratio (f), and the orientation angle (PA) of the galaxy (Kormann et al., 1994; Meneghetti, 2021). The position angle (PA) of the major axis of the ellipse is measured from North to East, where PA = 0 corresponds to a galaxy whose longest axis is aligned North-South.

To visualize the image positions of the source at $\mathbf{y}$ and $\mathbf{y}+\delta\mathbf{y}$, we have illustrated them in Figure 1. The positions corresponding to $\mathbf{y}$ are marked with "x", while those for $\mathbf{y}+\delta\mathbf{y}$ are indicated with "+". Since the number and location of images depend on the source's position relative to the caustic,

critical, and cut curves (Kormann et al., 1994; Meneghetti, 2021), we have also depicted these structures in the figure. The dashed orange line represents the caustic, the purple line denotes the critical curve, and the green line marks the cut. The lens is centrally positioned, with a quadruple quasar system shown on the left and a double quasar system on the right. The number and arrangement of images are determined by the source's location relative to these lensing structures. For a detailed discussion on image formation and positioning, refer to Meneghetti (2021) and the relevant literature.

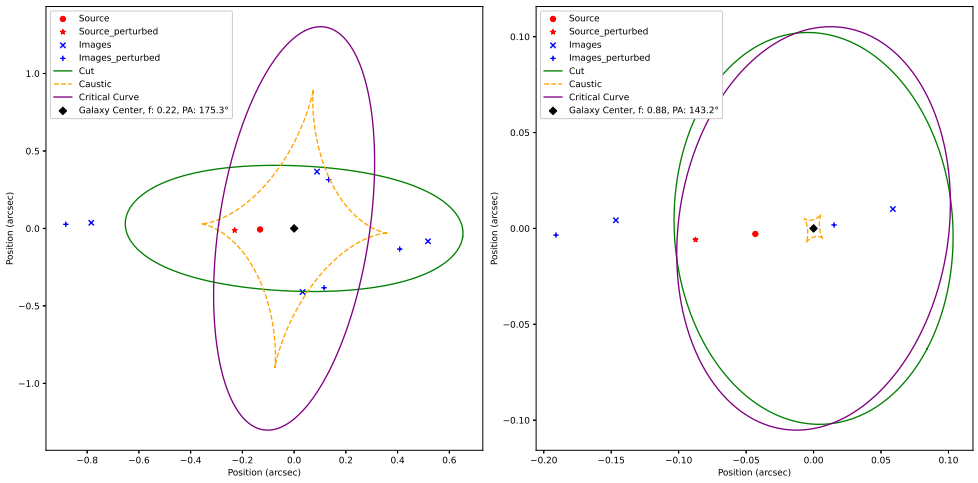

Fig. 1. In this figure we show the positions of the source (red dots and red stars) and lensed images (blue crosses and blue pluses) in arcseconds before and after the perturbation for quadruple and double quasars. The cut is represented by a green line, the caustic by a dashed orange line, and the critical curve by a purple line. The lens, marked by black diamond-shaped markers, is centrally positioned.

2. Simulations and Results

We have simulated strong lensing events following the general algorithm outlined in Hamolli et al. (2023a), introducing a modification by adjusting the quasar redshift distribution using data from the Million Quasars (Milliquas) catalog (Flesch, 2019). After constructing a sample of 10,000 lens-galaxy systems, we applied the angular resolution constraints of the Roman Space Telescope (0.1 arcsec) to filter out only those systems expected to be detectable. From this selection, 578 systems surpassed the detection threshold and were carried forward for further calculations. In our calculations, we continue to maintain the previously adopted values for cosmological parameters, assuming a flat Universe with $\Omega_m = 0.30$, $\Omega_k = 0.0$, $\Omega_\lambda = 0.70$, and $H_0 = 70$ km s^{-1} Mpc^{-1}.

For each event in the final sample, we solved the lens equation using the Singular Isothermal Ellipsoid (SIE) model for the lens galaxy. The required axial ratio (f) and position angle (PA) were extracted from the HyperLeda (Diameter Summary) catalog[3]. Our findings indicate that 468 quasars produced two images, 8 quasars resulted in three images, and 42 quasars generated four images. For each subsample—double, triple, and quadruple quasars—we determine the angular separation between the image pairs. Their distributions on a logarithmic scale are presented in Figure 2, where the left panel corresponds to quasars with two images, the middle panel represents quasars with three images, and the right panel displays quasars with four images. The bin width of 0.1 arcseconds (on logarithmic scale) is the same across all three panels, ensuring a clear comparison of the separation distribution. As observed, image separations are larger in the double-image and quadruple-image configurations.

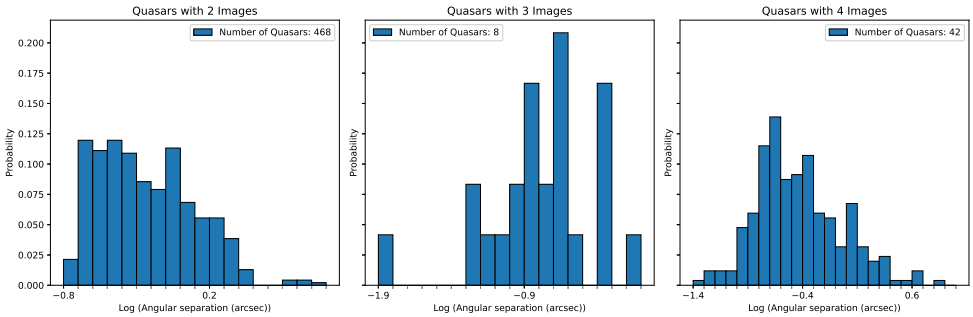

Fig. 2. The probability distribution of angular separations (on logarithmic scale) for lensed image pairs, shown in separate panels for double, triple, and quadruple quasars.

For each pair in the subsample, we calculate the time delays between the lensed images. The values range from 5.23 hours to 5.16 years for double quasars, 3.74 minutes to 2.3 days for triple quasars, and 1 minute to 200.3 days for quadruple quasars. To enhance visualization, we use a logarithmic scale to represent the probability distribution of each subsample. The bin width on this scale is set to 0.2 days, ensuring a clear and accurate depiction of the time delay distribution. Additionally, Figure 3 presents the probability distribution of time delays between lensed image pairs. The left panel corresponds to quasars with two images, the middle panel represents quasars with three images, and the right panel displays quasars with four images.

We further extend our investigation by calculating the time delay difference for each lensed quasar. To achieve this, we introduce a perturbation caused by a flare, with its distance r_c uniformly distributed within the range of 10 to 1000 pc. In each case, we repeat the choice of the lens equation, maintaining the same number of solutions. For the remaining events, we compute the time

[3] http://atlas.obs-hp.fr/hyperleda/a106/

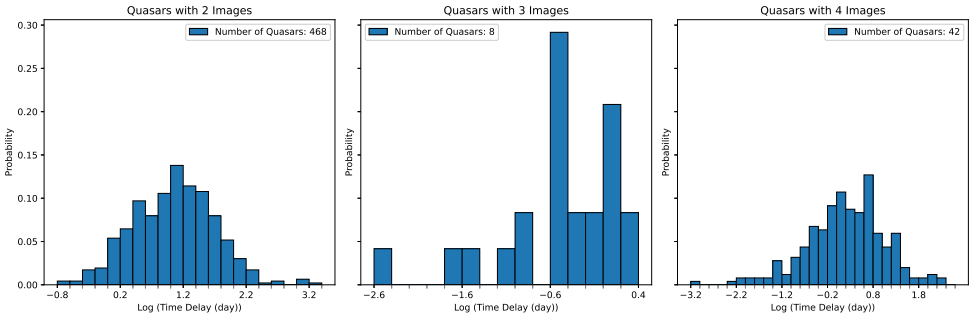

Fig. 3. The probability distribution of the time delays (on a logarithmic scale) between lensed image pairs for double, triple, and quadruple quasars.

delay differences and present their distribution on logarithmic scale in Figure 4.

To facilitate comparison, we set the bin width to 0.2 day on logarithmic scale for each case. The time delay differences range from 8.78 minutes to 73.45 days for double quasars, 1.15 minutes to 19.9 hours for triple quasars, and 17.3 seconds to 7.78 days for quadruple quasars, highlighting the correlation between the light curves of lensed image pairs.

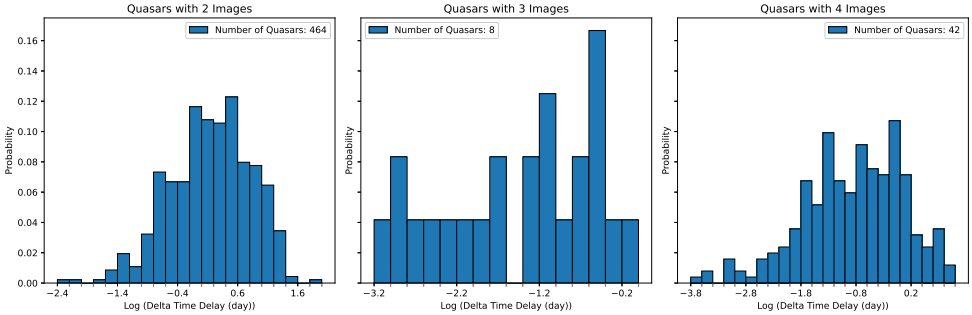

Fig. 4. The probability distribution of the time delay difference (on logarithmic scale) between lensed image pairs, classified into double, triple, and quadruple quasars.

As observed, double quasars exhibit larger time delay differences, which negatively impacts the correlation between their light curves. Given the 5-day imaging cadence of the Roman Space Telescope, we find that 104 out of 464 double quasars and 4 out of 42 quadruple quasars maintain a detectable correlation. The remaining events are significantly affected by intrinsic variability caused by flares.

Another key aspect of our investigation is to examine the relationship between the time delay variation and the size of the perturbation, focusing specifically on double quasars, as they represent the largest subset of events in our sample. To analyze this relationship, we generate a scatter plot of the time delay variation as a function of the burst distance (r_c), with our findings shown in Figure 5. In the same figure, we also show the probability distribution

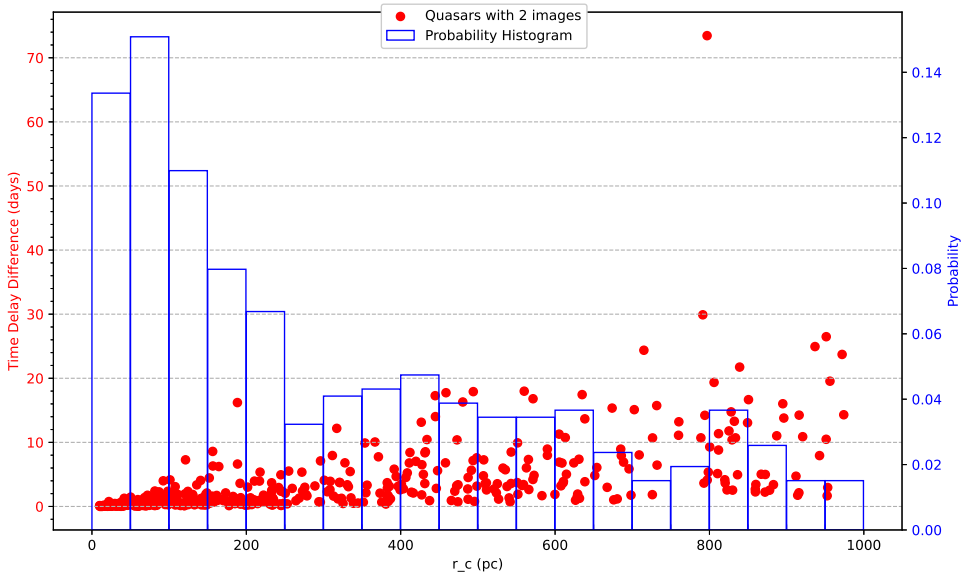

Fig. 5. A scatter plot (red dots) illustrates the relationship between the time delay difference of double quasars and the size of the perturbation in the SIE lens model. Alongside, a histogram (blue bars) represents the probability distribution of the burst distance (r_c) which range from 10 to 1,000 parsecs.

of bursts occurring at different distances r_c. As can be seen, their distribution is not uniform, although they are simulated as such, because distant source perturbations (bursts) are excluded when they change the number of lensed images. The scatter plot reveals a clear trend: as r_c increases, the change in time delay also tends to be larger, indicating that the perturbations caused by the explosion significantly affect the observed time delays. This tendency is further supported by both the Pearson correlation coefficient (0.59), which suggests a positive linear relationship, and the Spearman correlation coefficient (0.79), confirming a monotonic trend.

Conclusion

In this study, we examined the ability of the Roman Space Telescope to detect correlations in the light curves of lensed quasar images. Since quasars are

extended sources, their internal structure allows for various perturbations, particularly flare-induced variability, which can disrupt time-delay measurements in gravitational lensing studies.

By simulating strong lensing events using observed quasar redshift distributions and galaxy mass-luminosity functions, in a previous paper we have found that 85% of the quasars expected to be observed by Roman will be lensed by a galaxy (Hamolli et al. 2023b). Adopting a Singular Isothermal Ellipsoid (SIE) profile for them, we identified various image configurations, where the double quasars are more frequent.

We computed angular separations, time delays, and time delay differences for each lensing configuration, finding that double-image systems generally exhibit larger time delays and time delay differences compared to systems with three or four images. Given Roman's 5-day imaging cadence, we found that within a flare distance range of 10 to 1000 pc, time delay differences can be detected in 22.41% of double quasars and 9.52% of quadruple quasars. These multiple time delays introduce uncertainties in Hubble constant (H_0) measurements, potentially affecting precise determinations of cosmological parameters. These findings underscore the critical role of quasar variability in time-delay cosmography. As the Roman Space Telescope begins operations, future studies should integrate flare modeling, explore multi-wavelength monitoring, and apply advanced light curve decomposition techniques to improve the accuracy and reliability of time-delay measurements in lensed quasars.

References

Refsdal S., 1964, *Monthly Notices of the Royal Astronomical Society* 128, 4
Schechter P., 2004, *Proceedings of the International Astronomical Union* 225
Riess A., 2021, *The Astrophysical Journal* 908, 1
Aghanim N., 2020, *Astronomy & Astrophysics* 641, A6
Wong K., 2020, *Monthly Notices of the Royal Astronomical Society* 498
Oguri M., Marshall P.J., 2010, *Monthly Notices of the Royal Astronomical Society* 405, 4
Spergel D. N., 2015, *arXiv:1503.03757 [astro-ph.IM]*
Hamolli L., 2023a, *Galaxies* 11, 3
Guliqani E., 2024, *All Sciences Academy* ISBN: 978-625-6314-67-2
Vernardos G., 2014, *The American Astronomical Society* 211, 16
Yonehara A., 1998, *The Astrophysical Journal* 501, L41
Yonehara A., 1999, *The Astrophysical Journal* 519, 1
Bahcall J.N., 1997, *Astrophysical Journal* 479, 2
Goicoechea L. J., 2002, *Monthly Notices of the Royal Astronomical Society* 334, 4
Beaton R., 2023, *The American Astronomical Society* 55
Kormann R., 1994, *Astronomy and Astrophysics* 284
Meneghetti M., 2021, *Springer* 956
Hamolli L., 2024, *Journal of Natural Sciences* 35
Brent R. P., 1971, *The Computer Journal* 14, 4
Flesch E. W., 2019, *Astrophysics of Galaxies*
Hamolli L., 2023b, *Journal of Natural Sciences* 33